



HAL
open science

Perspectives on heterococcolith geochemical proxies based on high-resolution X-ray fluorescence mapping

Baptiste Suchéras-Marx, Fabienne Giraud, Alexandre Simionovici, Isabelle Daniel, Rémi Tucoulou

► **To cite this version:**

Baptiste Suchéras-Marx, Fabienne Giraud, Alexandre Simionovici, Isabelle Daniel, Rémi Tucoulou. Perspectives on heterococcolith geochemical proxies based on high-resolution X-ray fluorescence mapping. *Geobiology*, 2016, 14 (4), pp.390-403. 10.1111/gbi.12177 . hal-01419631

HAL Id: hal-01419631

<https://hal.science/hal-01419631>

Submitted on 8 Feb 2019

HAL is a multi-disciplinary open access archive for the deposit and dissemination of scientific research documents, whether they are published or not. The documents may come from teaching and research institutions in France or abroad, or from public or private research centers.

L'archive ouverte pluridisciplinaire **HAL**, est destinée au dépôt et à la diffusion de documents scientifiques de niveau recherche, publiés ou non, émanant des établissements d'enseignement et de recherche français ou étrangers, des laboratoires publics ou privés.

Perspectives on heterococcolith geochemical proxies based on high resolution X-ray fluorescence mapping

B. Suchéras-Marx^{a,b,c,*}, F. Giraud^{d,e}, A. Simionovici^{d,e}, I. Daniel^a, R. Tucoulou^f

^a UMR CNRS 5276 LGL, Université Claude Bernard Lyon 1, Ecole Normale Supérieure Lyon, Campus de la Doua, 69622 Villeurbanne Cedex, France

^b Université de Lyon, Université Jean Monnet and UMR-CNRS 6524, Laboratoire Magmas et Volcans, 23 rue du Dr Paul Michelon, 42023 Saint Etienne, France

^c CEREGE UM34, Aix-Marseille Université, CNRS, IRD, 13545 Aix-en-Provence, France

^d Université Grenoble Alpes, ISTERre, F-38041 Grenoble, France

^e CNRS, ISTERre, F-38041 Grenoble, France

^f ESRF – The European Synchrotron, CS 40220, 38043 Grenoble Cedex 9, France

* Correspondence to: B. Suchéras-Marx sucheras-marx@cerege.fr; baptiste.sucheras@gmail.com; tel:+33 (0)4 42 97 15 83; fax: +33 (0)4 42 97 15 05.

ABSTRACT

Heterococcoliths are micron-scale calcite platelets produced by coccolithophores. They have been the most abundant and continuous fossil record over the last 215 million years (Myr), offering great potential for geochemical studies, although the heterococcolith fossil record remains underutilised in this domain. We have mapped heterococcoliths' composition using X-ray fluorescence (XRF) with a 100 nm resolution beam in order to decipher element distributions in heterococcoliths and to investigate the potential development of geochemical proxies for palaeoceanography. The study presents two Middle Jurassic *Watznaueria britannica* heterococcoliths from Cabo Mondego, Portugal. XRF analysis was performed with a 17 keV incident energy beam at the European synchrotron radiation facility ID22NI beamline in order to study elements from Sr down to S. Ca, Sr and Mn are distributed following the heterococcolith crystalline arrangement. Cl, Br and S display an homogeneous distribution, whereas K, Fe, Cu, Zn and Rb are concentrated at the edges and in the central area of the heterococcoliths. Distributions of K, Fe, Ti, Fe, Cu, Zn, Rb, and to a lesser extent V and Cr, are highly influenced by clay contamination and peripheral diagenetic overgrowth. Mn is related to diagenetic Mn-rich CaCO₃ overgrowth on top of or between heterococcoliths shields. Cl and Br are likely to be present in heterococcoliths inside interstitial nano-domains. We assume that the cytoplasm [Cl⁻] and [Br⁻] are mediated and constant during heterococcolithogenesis. Assuming a linear correlation between cytoplasm [Cl⁻] and seawater [Cl⁻], heterococcolith Cl may have potential as a salinity proxy. As S is incorporated into heterococcoliths by sulphated polysaccharides, and our study suggests a role for such polysaccharides in heterococcolithogenesis for at least 170 Myr. The low Sr/Ca in the *W. britannica* specimens studied here may either highlight an unusual cellular physiology of Mesozoic coccolithophores or result from low growth rates in oligotrophic environments.

INTRODUCTION

Coccoliths are micron-size platelets (< 15 µm) produced by the golden-brown algae coccolithophores. They are the most abundant calcareous nannofossils in marine sediments from coastal to open-ocean environments over the last 215 Myr (e.g. Winter & Siesser, 1994;

Bown, 1998; Thierstein & Young, 2004). Coccoliths are produced inside the cell and then extruded through the cell membrane to cover the cell (Taylor *et al.*, 2007), forming an exoskeleton with multiple interlocking coccoliths called a coccosphere. Two types of coccoliths are distinguished: i) holococcoliths, which are produced during the haploid phase of the coccolithophore life-cycle and ii) heterococcoliths, which are produced during the diploid phase (e.g. Geisen *et al.*, 2002). In the fossil record, heterococcoliths far outnumber holococcoliths, probably because they have greater preservation potential and/or different ecological preferences (Dunkley Jones *et al.*, 2009; Cros & Estrada, 2013).

Heterococcoliths are generally made of very low Mg-calcite (Mg/Ca = 0.1-0.2 mmol/mol; Stoll *et al.*, 2001). Low Mg-calcite is relatively resistant to dissolution in deep cold seawater because of its thermodynamic properties (Schlanger *et al.*, 1973). As a consequence, heterococcoliths are well preserved in the geological record. However, because of their very small size (2 to 15 μm in diameter), and extremely low mass (5 to 650×10^{-12} g), analysing their chemical composition remains difficult, and fossil heterococcoliths are seldom used as a geochemical proxy substrate for palaeoceanography, compared to planktic foraminifera that are commonly used.

Studies of heterococcolith geochemistry first emerged in the late 1970's (e.g. Siesser, 1977; Dudley & Goodney, 1979; Dudley *et al.*, 1986) and the number of such studies has grown over the past fifteen years (see review by Stoll & Ziveri, 2004), as it became possible to separate heterococcoliths from bulk sediment (Stoll & Ziveri, 2002; Minoletti *et al.*, 2009; Stoll & Shimizu, 2009) and analyse single heterococcoliths (Stoll *et al.*, 2007a; Prentice *et al.*, 2014). Several geochemical proxies based on heterococcoliths are now calibrated, such as temperature proxies based on $\delta^{18}\text{O}$ (Candelier *et al.*, 2013), Mg/Ca (Ra *et al.*, 2010) or 'clumped isotopes' (Tripathi *et al.*, 2010); seawater composition proxies based on Mg concentration and Mg/Ca (Stanley *et al.*, 2005; Müller *et al.*, 2011), and productivity proxies based on Sr/Ca (Stoll & Schrag, 2000; Rickaby *et al.*, 2002; Stoll & Bains, 2003). However, with the exception of the recent study by Prentice *et al.* (2014), heterococcolith geochemistry still lacks high spatial resolution studies that help to understand element incorporation mechanisms (e.g. for foraminifera (Sadokov *et al.* 2005)). In the present study, we analyse the chemical composition of single heterococcoliths at 100 nm spatial resolution using synchrotron X-ray fluorescence (XRF). The heterococcoliths analysed are two 170 Myr-old *Watznaueria britannica* heterococcoliths from Cabo Mondego, Portugal. *W. britannica* is an elliptical imbricated placolith made of several *c*-axis calcite single crystals and is abundant in middle Jurassic to Cretaceous deposits (Fig. 1A-B). The high-resolution 2D mapping allows us to discuss the distribution of elements, deduce mechanisms of elemental incorporation in heterococcoliths, and propose new perspectives on heterococcolith geochemistry.

MATERIAL AND METHODS

Heterococcolith samples and picking

W. britannica heterococcoliths were picked from a Cabo Mondego (Portugal) marlstone sample (CM62 in Suchéras-Marx *et al.*, 2012), and are dated to the Propinquans ammonite Zone in the Early Bajocian (Middle Jurassic, ca 170 Ma). This sample was selected because of the high abundance of well-preserved heterococcoliths, with overgrowth only observed under the SEM (Fig. 1B). The marlstone sample was powdered in an agate mortar using a

power hammer. A smear slide (Bown & Young, 1998) was then prepared with ethanol. Heterococcoliths were separated from the bulk sample following a picking method modified from Stoll & Shimizu (2009), using a 150 μm silicate tube thinned down to $\sim 15 \mu\text{m}$ diameter by stretching in a flame. Individual heterococcoliths were picked by hand from the smear slide and deposited on sample holders using a Leica DM750P microscope at 400x magnification. Samples were mounted on 500 nm thick silicon nitride (Si_3N_4) TEM windows (Silson Ltd.). A droplet of ethanol deposited on the window helped to detach the heterococcolith from the silicate tube by surface tension. The *W. britannica* heterococcoliths presented in this study are called Wbrit1 and Wbrit2.

Synchrotron radiation X-ray Fluorescence

XRF measurements were performed at the European synchrotron radiation facility (ESRF), Grenoble, France on the beamline ID22NI. The XRF method is based on the excitation of elements by high energy X-rays. Due to the incident X-ray excitation, elements present in the sample emit secondary X-rays with constant energies per element and intensities depending on the concentration of each element. The incident X-ray beam energy was set at 17 keV to ensure the measure of Sr ($K\alpha = 14.165 \text{ keV}$) and lighter elements. ID22NI uses an ESRF custom-made Kickpatrick-Baez double multilayer mirrors device focusing the X-rays into a beamspot of $100 \text{ nm} \times 100 \text{ nm}$. Analysis spots are adjacent, without overlapping or leaving space between two spots. The detectors were high-count rate twin SIITM Vortex SDD (silicon drift diodes) detectors, capable of counting up to 200 kcps with no saturation and no peak shift or FWHM broadening, when operated below 10% dead time. Heterococcoliths were analysed with 2 s dwell time per pixel.

The Wbrit1 map was 81×71 pixels ($\sim 3 \text{ h } 15$) and the Wbrit2 map was 85×65 pixels ($\sim 3 \text{ h}$). The sample is orthogonal to the incident beam and the detector is located at a 15° angle relative to the sample surface. XRF is a penetrative method and one pixel sums the fluorescence signal throughout the whole heterococcolith thickness, the TEM windows and the air on both sides of the sample. The TEM windows were homogeneous in all the elements analysed and the air composition did not interfere with measured heterococcolith composition. The set up geometry influences the mapping results. The maps will give an image, which depends on the excitation angle *i.e.* orthogonal to the heterococcoliths shields in our set up. The intensity of photons per element depends on the concentration and the thickness of the analysed material. If the heterococcoliths have homogeneous composition, the thickness influence can be excluded because it would be the same for all elements. However, in case of layers with higher or lower concentrations in a given element inside or over (*i.e.* overgrowth crust) a heterococcolith, the thickness of the layer is a key parameter, which should be considered in the interpretations. Elemental mapping of the NIST 1577b Bovine Liver standard was performed under similar conditions in order to calibrate the exact analytical geometry. The fitted spectrum was constructed using the sum of photons for all heterococcolith pixels divided by the number of pixels, and the fitting calculations were made pixel by pixel. Fits were performed using the PyMCA 5.7.0 (Solé *et al.*, 2007) software, which uses the Hypermet function coupled with the standard Levenberg-Marquardt non-linear fitting method. Peaks were routinely fitted by a least squares procedure, using Poisson weights based on their surfaces. The lines used in the fitting procedure are $K\alpha$ and $K\beta$ lines –

the main transition lines from orbitals with principal quantum number $n=2$ and 3 to $n=1$ – and also $L\alpha$ and $L\beta$ – main transition lines from orbital $n=3$ to $n=2$ lines. Absolute minimum detection limits (MDL) at ID22NI estimated in the standard 1000 s interval are 20-70 zg ($2-7 \times 10^{-20}$ g) for intermediate Z elements. When mapping with a 1 s dwell time, the absolute MDL is approximately 1-2 fg, whereas relative limits are 1-2 ppm for Cr-Cu. PyMCA was also used to calculate the relative molar fraction of element i to calcium Ca (i/Ca ; mmol/mol).

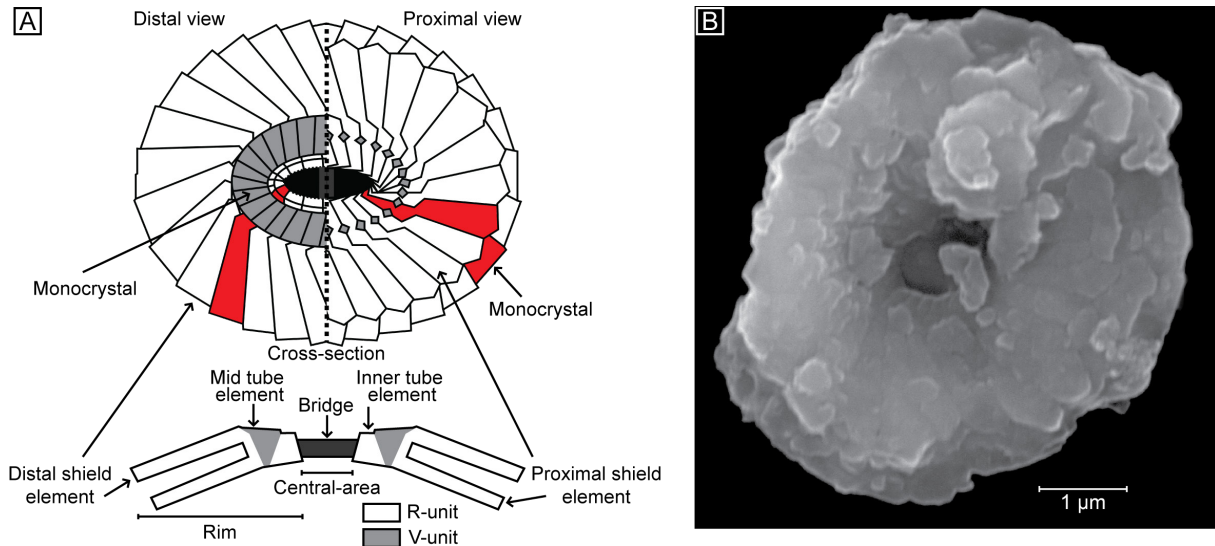


Figure 1: A) Crystal organisation of *W. britannica* (derived from Young & Bown, 1991) in distal and proximal view and in cross-section. *W. britannica* is an elliptical imbricated placolith, the long axis of the ellipse is perpendicular to the central area bridge and called major axis; the axis perpendicular to the major axis is called the minor axis. *W. britannica* is made of several c -axis elongated calcite monocrystals organised in two shields – forming the rim – connected by a central inner tube partly filled by a bridge. The shield in contact with the cell in life position is called proximal shield, the other one is called distal shield. The shields are made in the outer part and most inner part of calcite crystals with a radial growth direction (from the centre to the edge) intersected by crystals with a vertical growth direction (from the proximal to the distal shield). In proximal view, the calcite crystals of the proximal and distal shields are imbricated anti-clockwise (laevogyre) and clockwise (dextrogyre), respectively. B) SEM picture of a *W. britannica* from the same rock sample of the heterococcoliths analysed in this study. The heterococcolith is presented in proximal view allowing the observation of the crystal organisation of the proximal shield.

Calculation of relative ratio i/Ca

Relative ratio tables and maps for the two heterococcoliths are shown in the results section, and show the concentration of element i with respect to the major element Ca. This procedure of normalisation allows correcting the element intensity for the sample thickness effect. The constant contribution of the TEM Si_3N_4 windows to the concentration values for each element was subtracted. The trace element composition of the TEM windows in element i was calculated as the median of the concentration of element i in all pixels void of heterococcolith contribution, *i.e.* around the heterococcolith. We use the median value rather than the arithmetic mean because it is less affected by potential outliers. Ratios are expressed in mmol/mol. The cut-off threshold contouring heterococcoliths was set for $[\text{Ca}] = 3 \times 10^4$ cps

and Ca ratios have been arbitrarily set to 0 below the latter threshold value. In Table 1, three regions of interest (ROI) are presented, the whole heterococcolith (Full), a region depleted in K, Fe, Cu, Zn and Rb (ROI 1) and a region more concentrated in K, Fe, Cu, Zn and Rb (ROI 2). Each ratio corresponds to the arithmetic mean of pixels in the ROI; the arithmetic mean is used because it is sensitive to the variance and allows more easily discussing the effect of outliers on heterococcoliths bulk composition (Full vs ROI 1 and ROI 2).

Elemental ratio (mmol/mol)	Wbrit1			Wbrit2		
	Full	ROI 1	ROI 2	Full	ROI 1	ROI 2
S/Ca	4.843	3.776	1.745	3.656	1.257	1.029
Cl/Ca	20.935	15.701	19.756	17.215	16.193	14.593
K/Ca	12.325	0.877	24.946	6.703	0.122	8.098
Ti/Ca	1.091	<0.001	1.623	0.943	0.021	0.227
V/Ca	0.111	<0.001	0.044	0.114	<0.001	0.003
Cr/Ca	0.068	<0.001	0.028	0.078	0.006	0.010
Mn/Ca	0.961	0.820	1.328	0.784	0.803	0.998
Fe/Ca	9.750	2.126	18.884	8.756	1.781	7.842
Cu/Ca	0.361	0.044	0.483	0.334	0.035	0.340
Zn/Ca	0.495	0.12	0.907	0.914	0.182	0.759
Br/Ca	0.013	0.008	0.006	0.018	0.015	0.014
Rb/Ca	0.022	<0.001	0.046	0.012	<0.001	0.011
Sr/Ca	0.351	0.365	0.334	0.360	0.389	0.339

Table 1: Wbrit1 and Wbrit2 elemental ratio (mmol/mol) of the whole heterococcolith (Full), in overgrowth-free region (ROI 1) and in overgrown region (ROI 2). Selected region of interest are presented in Fig. 6.

RESULTS

Elemental spectrum

The XRF spectrum displays the K-lines of 16 elements (Fig. 2), namely S, Cl, Ar, K, Ca, Ti, V, Cr, Mn, Fe, Cu, Zn, Br, Kr, Rb, Sr. The L-lines of Pb are also identified in the XRF spectrum. Due to the incident excitation beam energy of 17 keV, no element heavier than Sr has been identified aside from Pb. At low energy, the setup at ID22NI in air does not allow measuring elements lighter than S. Ar and Kr observed in the spectrum are from the air in the experimental hutch. Traces of Pb are usually considered as contamination, since high-energy experimental hutches at the ESRF are shielded with Pb. The least intense K-line identified, namely Cr K-line, is still about 30 times higher than the MDL. XRF is a penetrative method such that the incident beam goes across the sample with negligible absorption (≤ 0.004) while the fluorescent lines feature moderate self-absorption (corrected) as a function of their energy and exit angles in the sample. The Mn $K\alpha$ -line features roughly 12% absorption in a 3 μm CaCO_3 sample while Ca displays features between 12% and 45% absorption. This progressive absorption as a function of the exit angle is a smooth dependence, which affects only the low Z element lines such as those of S, Cl, K and Ca. This dependence does not produce a visible effect on the element distribution but affects the whole map by underestimating the pixel values, which contain a partial grazing exit contribution. Hence, 14 trace elements were successfully identified and mapped in *W. britannica*.

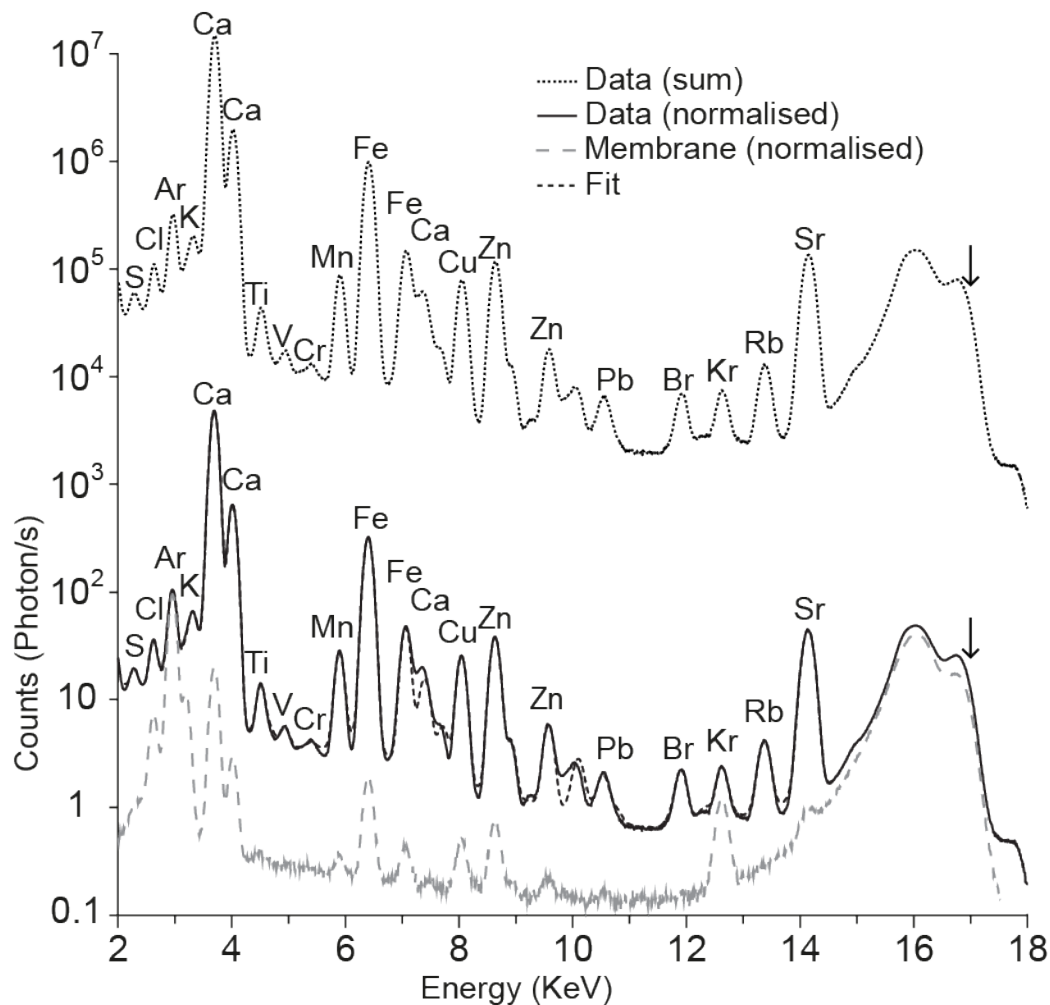


Figure 2: XRF spectrums with i) Data (sum) corresponding to the sum of all pixels within *W. britannica* Wbrit1, ii) Data (normalised) corresponding to the sum of all pixels normalised by the number of pixels within *W. britannica* Wbrit1, iii) Membrane corresponding to the sum of all pixels normalised by the number of pixels within the TEM window holding the heterococcolith, and iv) Fit corresponding to the fit calculated with PyMCA and used for calculating the concentration of element *i* relative to Ca (i/Ca) in Table 1 and Figs. 7 to 9.

Elemental maps

To clearly present the 14 elemental maps produced, they were separated in three groups based on a comparison between their 2D distribution and the morphology of *W. britannica*. The results in cps are presented in Figs. 3-5 with thresholds applied (see captions) in order to observe the distinctive details. The full datasets are presented on a log-scale in Supplementary Material 1 for Wbrit1 and Supplementary Material 2 for Wbrit2.

Group 1: morphological distribution (Ca, Sr and Mn)

Results for Ca, Sr and Mn are presented in Fig. 3. The Mn map in Wbrit1 shows 2 concentric rings, the wider outer ring is composed of radial features whereas the inner ring is very narrow, about 200 nm wide. In Wbrit2, only the external ring is clearly observed. The central parts of both heterococcoliths are almost entirely Mn-free. The Sr maps for both Wbrit1 and Wbrit2 show 2 concentric rings with radial features. The Sr outer ring is superimposed on the

Mn outer ring whereas the Sr inner ring has a slightly larger diameter than the Mn inner ring. On Ca maps, radial features are clearly visible in the outer ring and continue towards the central area. The central area of the heterococcoliths contains less Ca and Sr than the shield.

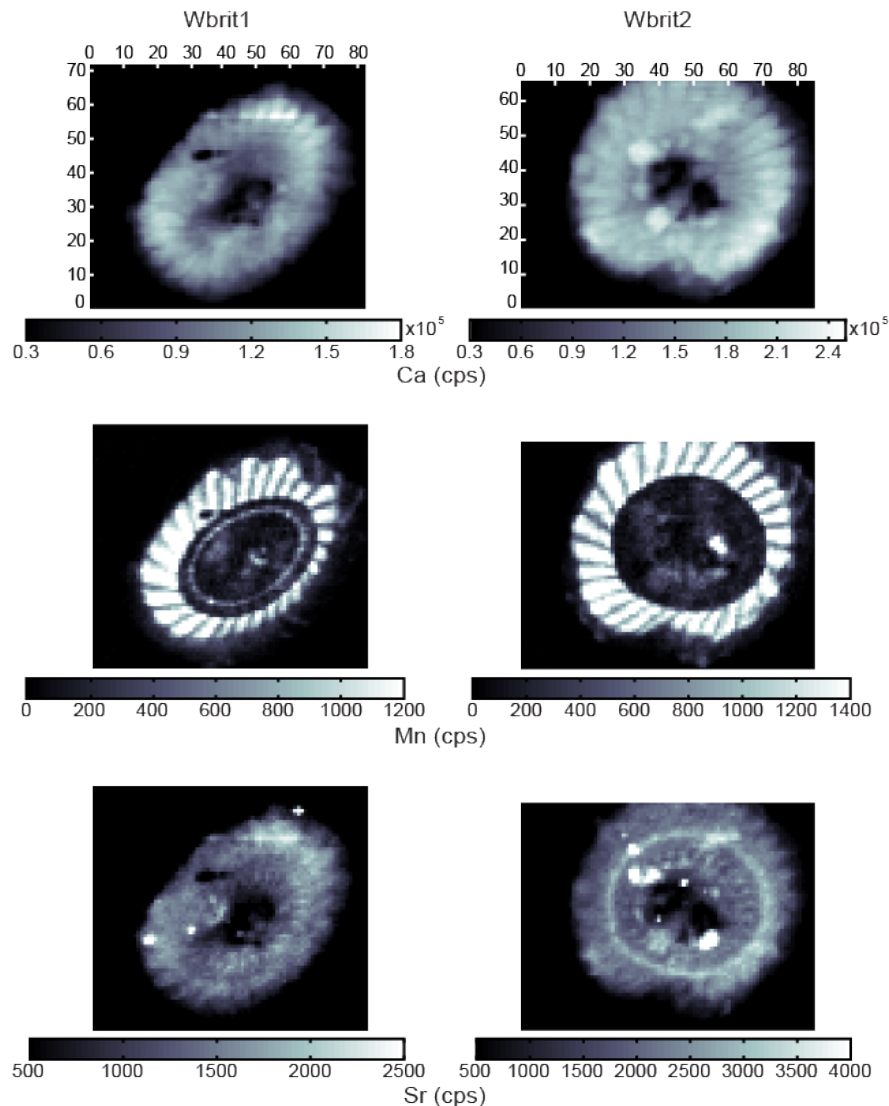


Figure 3: Elemental maps of Ca, Mn and Sr presented in photon counts per second (cps). Scales do not display the full range of values, thresholds are set to offer a better observation of the organisation.

Group 2: homogeneous distribution (S, Cl, Br, Ti, V, Cr)

Results for S, Cl, Br, Ti, V and Cr are presented in Fig. 4. S, Cl, Br and to a lesser extent Ti, V and Cr have an homogeneous distribution. Cl and Br have a very similar elemental distribution, whilst Br is less abundant. S does not show any organisation apart from a discontinuous ring with variable width that is slightly more concentrated. S is slightly less abundant in the central area and its distribution is more similar to Br than Cl. Cr and V have very similar elemental distributions, quite homogenous except for a zone of higher concentration close to the centre of the heterococcolith. Finally, Ti has an overall low abundance, but in ~15 spots ranging in size from 100 to 500 nm in which Ti concentration is very high. However, the Ti map drawn in log-scale displays a 2D distribution that is very similar to that of Cr and V except for the highly enriched spots (Supplementary material 1 and 2).

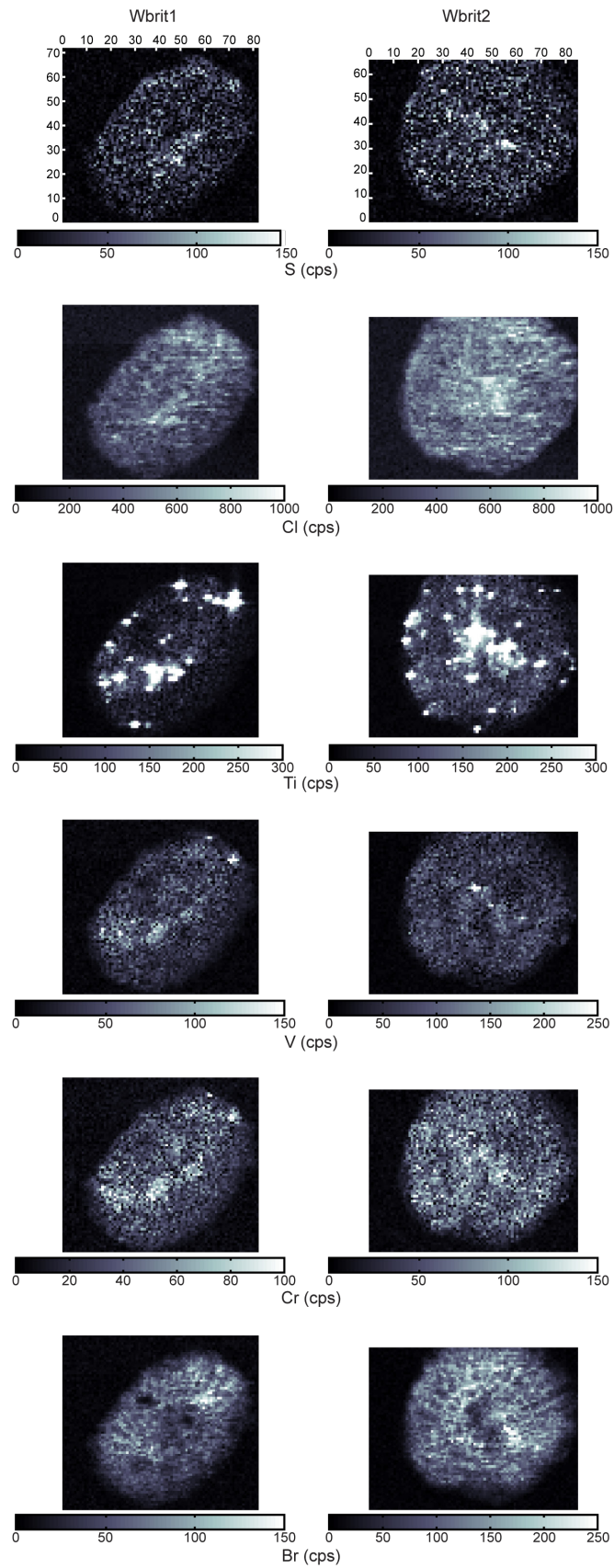


Figure 4: Elemental maps of S, Cl, Ti, V, Cr and Br presented in photon counts per second (cps). Scales do not display the full range of values, thresholds are set to offer a better observation of the organisation.

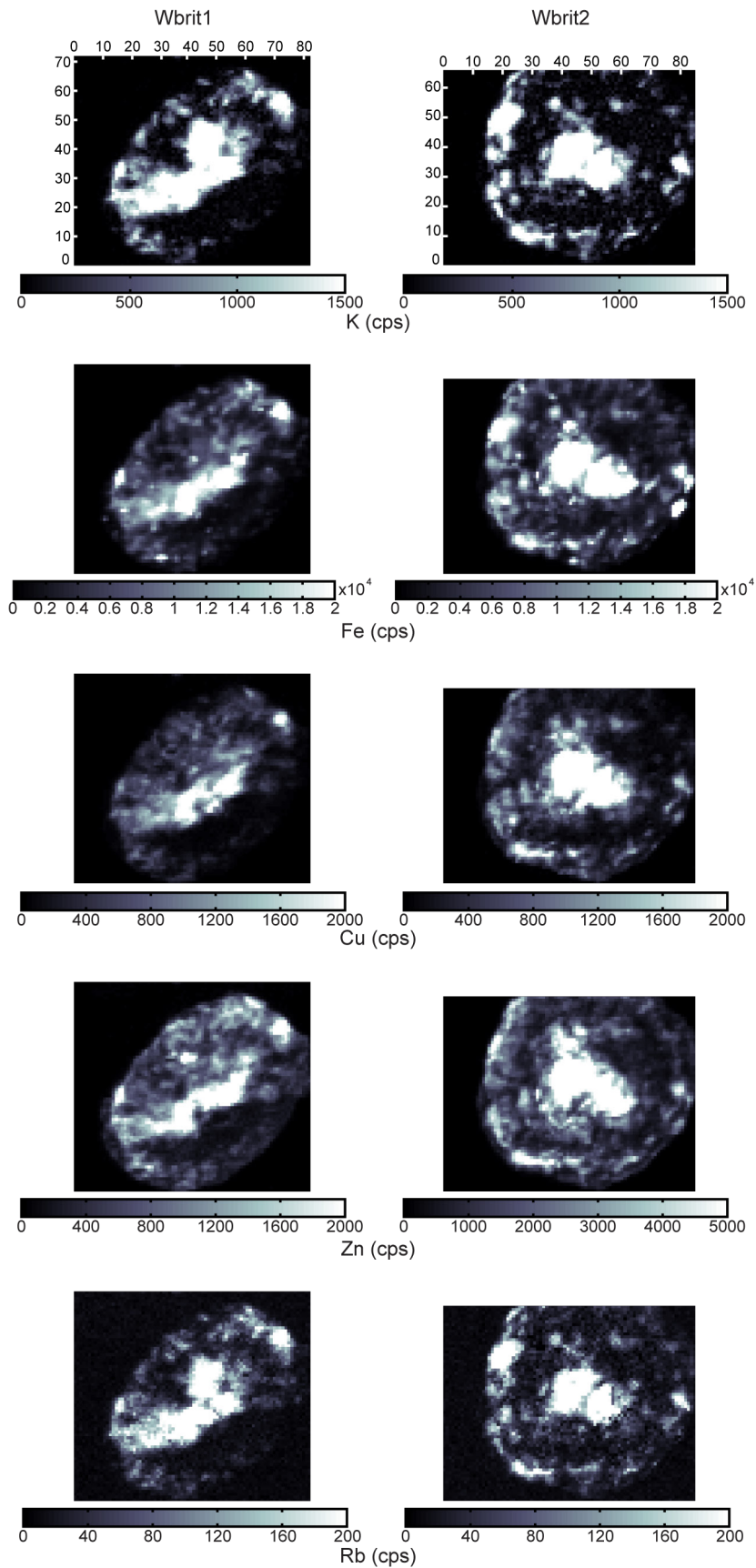


Figure 5: Elemental maps of K, Fe, Cu, Zn and Rb presented in photon counts per second (cps). Scales do not display the full range of values, thresholds are set to offer a better observation of the organisation.

Group 3: peripheral and central distribution (K, Fe, Cu, Zn, Rb)

Results for K, Fe, Cu, Zn and Rb are presented in Fig. 5. The distributions of these elements are very similar. They are highly concentrated on the external edge of the heterococcolith and in an area that covers the centre and extends along the heterococcolith's major axis. All these elements present comparable 2D distributions, however Rb and K are most similar to each other and Fe is similar to Cu and Zn.

Element/Ca relative concentrations and maps

Relative concentration

Relative concentrations of 13 elements normalised to Ca, hereafter designated as i/Ca ratios, are presented in Table 1, with the relative concentrations for the whole heterococcolith (Full) and for labelled regions of interest (ROI 1 and 2) (Fig. 6) shown. Maps of i/Ca ratios (in mmol/mol) are presented in Figs. 7-9.

In Table 1, the first column gives the mean i/Ca ratio for the whole heterococcolith; the second column labelled ROI 1 corresponds to the mean i/Ca ratio for a zone depleted in K, Fe, Cu, Zn and Rb. The last column labelled ROI 2 corresponds to the mean i/Ca ratio for a zone enriched in K, Fe, Cu, Zn and Rb. ROI 2 was selected because of the presence of metals identified in previous studies on calcite shells as contaminants (Pena *et al.*, 2008; Prentice *et al.*, 2014) while ROI 1 represents a more pristine section of the heterococcolith.

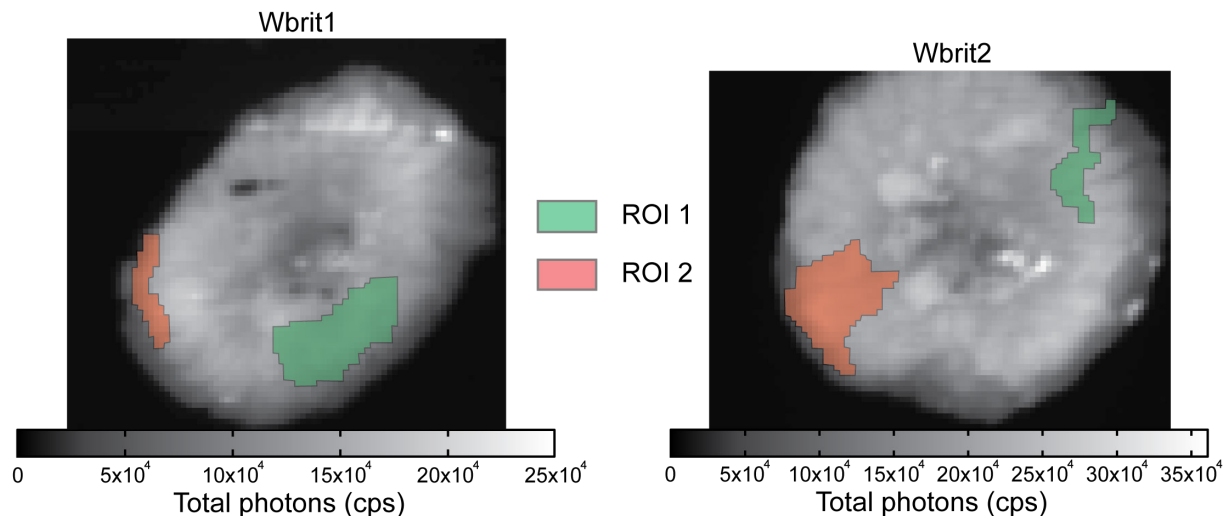


Figure 6: Localisation of ROI 1 and ROI 2 in Wbrit1 and Wbrit2.

The highest mean elemental ratios are observed for Cl/Ca, K/Ca and Fe/Ca. V/Ca, Cr/Ca, Br/Ca and Rb/Ca have very low elemental ratios, often below 0.1 mmol/mol, in the part per million range.

The comparison of i/Ca ratios between the whole heterococcolith and the selected ROI 1 and ROI 2 zones reveals two major features. i) Sr/Ca, Mn/Ca and Br/Ca have very comparable relative concentrations, ii) K/Ca, Ti/Ca, V/Ca, Cr/Ca, Fe/Ca, Cu/Ca, Zn/Ca, Rb/Ca are less abundant in ROI 1 than in the whole heterococcolith and ROI 2. In most case, i/Ca ratios in ROI 2 are similar to or very close to the mean values in the whole heterococcolith. Finally, in

Wbrit2, S/Ca and Cl/Ca are higher in ROI 1 than in ROI 2 and the whole heterococcolith whereas Br/Ca ratios are constant between ROI 1, ROI 2 and the whole heterococcolith.

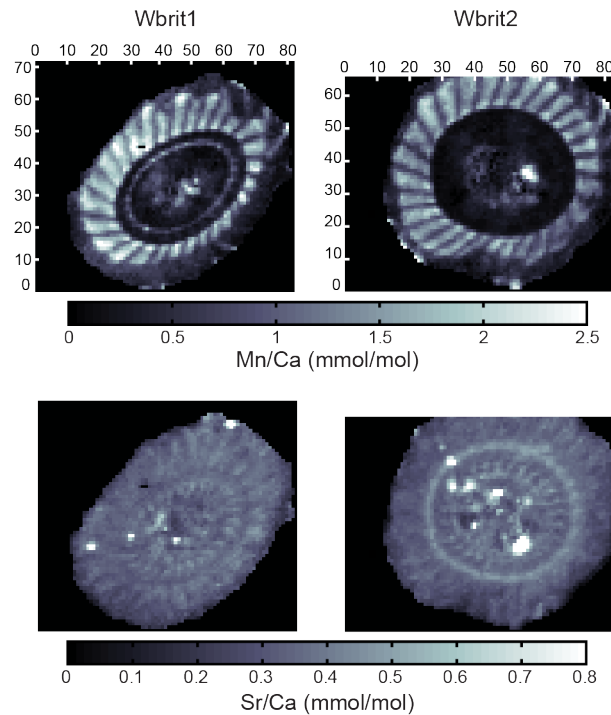


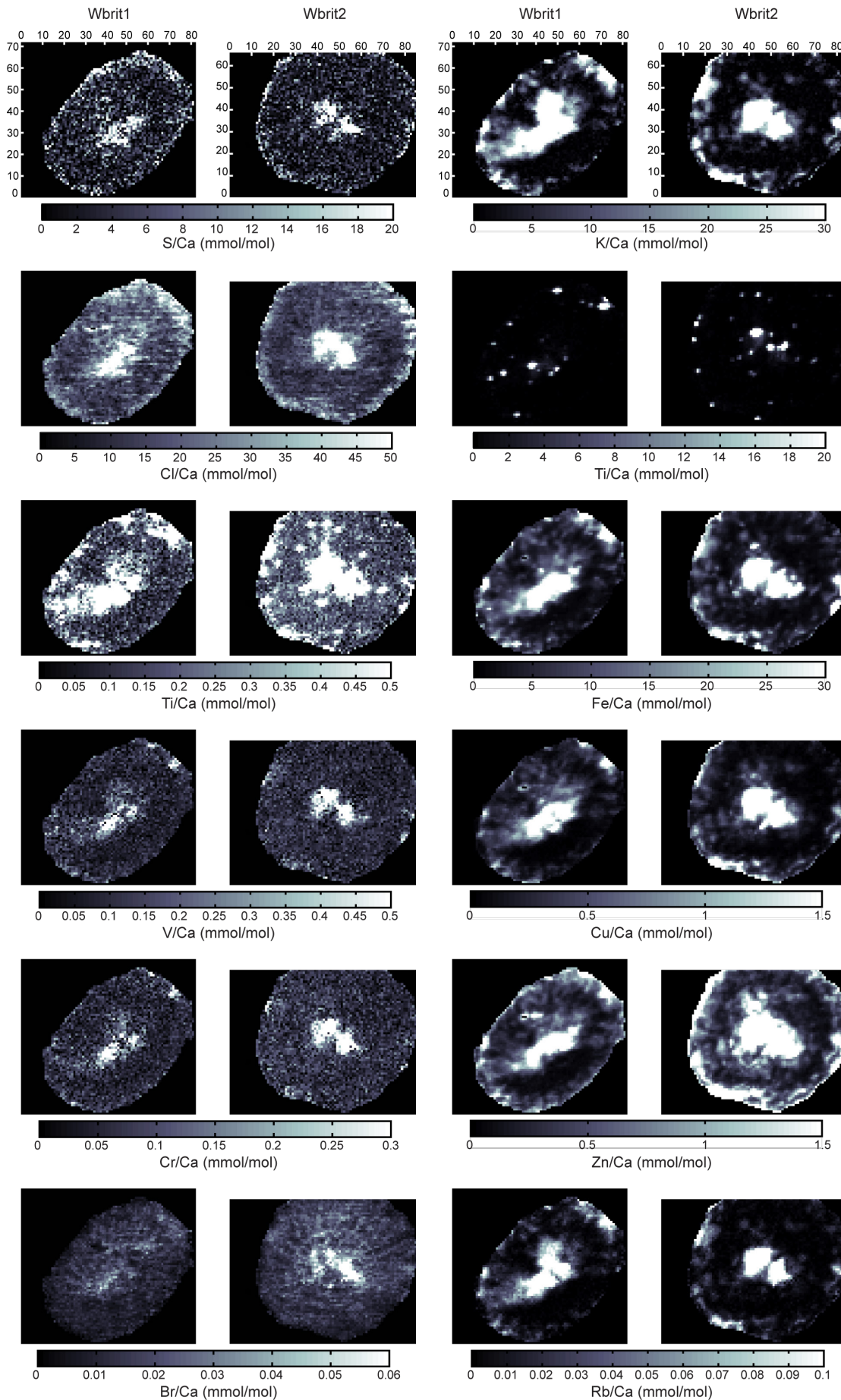
Figure 7: Ratio maps of Mn/Ca and Sr/Ca presented in mmol/mol. Scales do not display the full range of values, thresholds are set to offer a better observation of the organisation.

Group 1: morphological distribution (Sr/Ca and Mn/Ca)

Results for Sr/Ca and Mn/Ca are presented in Fig. 7. Mn/Ca display exactly the same distributions as the Mn elemental maps, two concentric rings with pronounced radial structures in the outer ring in Wbrit1 and an outer ring with radial structures in Wbrit2. In Wbrit1 and Wbrit2, the radial structures of the external ring are marked by the alternation of high and low Mn/Ca. The Sr/Ca maps display a complex organisation in both heterococcoliths. In Wbrit1, Sr/Ca is organised in three concentric rings, with the external and the internal ones separated by a ring with lower Sr/Ca. In Wbrit2, four concentric rings are observed, with a supplementary ring located between the external ring and the intermediate depleted ring. This extra ring is very thin (i.e. ~200-300 nm) with high Sr/Ca. The Sr/Ca rings described on both heterococcoliths systematically display radial features.

Group 2: homogeneous distribution (S/Ca, Cl/Ca, Br/Ca, Ti/Ca, V/Ca, Cr/Ca)

Results for S/Ca, Cl/Ca, Br/Ca, Ti/Ca, V/Ca and Cr/Ca are presented in Fig. 8. All element ratios i/Ca in this group present artificially very high values in the central area due to the presence of a hole. In both heterococcoliths, the S/Ca ratio is very homogeneous and Cl/Ca and Br/Ca are very similar, displaying a homogenous pattern with some weak radial features. V/Ca and Cr/Ca display a general homogenous pattern with small zones that are highly enriched. Lastly, the Ti/Ca distribution is patchy with a few small, very Ti-rich zones (i.e. ~200-700 nm) and a general pattern that is similar to those of V/Ca and Cr/Ca ratios.



Left - Figure 8: Ratio maps of S/Ca, Cl/Ca, Ti/Ca, V/Ca, Cr/Ca and Br/Ca presented in mmol/mol. Scales do not display the full range of values, thresholds are set to offer a better observation of the organisation.

Right - Figure 9: Ratio maps of K/Ca, Ti/Ca, Fe/Ca, Cu/Ca, Zn/Ca and Rb/Ca presented in mmol/mol. Scales do not display the full range of values, thresholds are set to offer a better observation of the organisation.

Group 3: peripheral and central distribution (K/Ca, Fe/Ca, Cu/Ca, Zn/Ca, Rb/Ca, Ti/Ca)

This third group composed of K/Ca, Fe/Ca, Cu/Ca, Zn/Ca and Rb/Ca elemental ratios is characterised by maps showing a relative enrichment in the centre and outer edge of heterococcoliths (Fig. 9). In the *i*/Ca maps of group 3, an elongated, enriched zone along the major axis (larger than the central area) is located in the centre of the heterococcoliths. Radial features are sometimes observed and are more pronounced in Wbrit1 than in Wbrit2. In Wbrit1 Cu/Ca, Zn/Ca and Fe/Ca, on the bottom part of the maps, those radial structures are closer to the heterococcolith external border than to the centre. But on the upper and left parts of the maps, the radial structures seem longer, radiating from the external border almost to the centre. In Wbrit2 Fe/Ca, Cu/Ca, Zn/Ca and Rb/Ca, there are fewer radial structures radiating from the heterococcolith external border to a depleted zone. Ti/Ca is also classified as group 3 because despite a generally homogenous pattern, it presents several spots with high Ti/Ca relative concentration as mentioned earlier.

DISCUSSION

Post-depositional overprint on the heterococcolith composition

Clay contamination

We consider as contamination any particle that was not originally a piece of the heterococcolith. We tried to minimise contamination from the matrix rock by using the careful picking method developed in the present study. In sedimentary carbonate deposits, contaminants could be either carbonate from the matrix (e.g. broken pieces of shells and tests), siliciclastic particles (e.g. clay, quartz) or organic matter (OM). In both heterococcoliths Wbrit1 and Wbrit2, the centre of the heterococcoliths is contaminated. This zone is depleted in Ca but highly enriched in K, Fe, Cu, Zn and Rb (Figs. 3 and 5). This contamination cannot be due to broken pieces of carbonate because Ca concentration is low. We also exclude the presence of micrometric grains of quartz because they were not observed in sample CM62 (see sample localisation in Suchéras-Marx *et al.*, 2012). We also exclude bulk algal organic matter contamination because such organic matter is composed of Fe and Mn (Ho *et al.*, 2003) and we only observe Fe and almost no Mn in the central area. We therefore confidently attribute this contamination to clay particles from the marlstones from which heterococcoliths were picked. Clays are generally composed of Si, Al, Fe, Mg, Ca, Na, and K as major elements, and contain traces of Ti, Cr, Cu, Zn, Rb and Sr (Köster, 1996); they are typically depleted in Ca and Sr in comparison to heterococcoliths (Stoll & Ziveri, 2004). High Fe/Ca was already proposed as a way to identify clay contamination in heterococcolith geochemistry studies (Halloran *et al.*, 2009); with clay contamination being later confirmed by atomic force microscopy observations of sub-micron clay particles covering

heterococcoliths (Skovbjerg *et al.*, 2012) and secondary ion mass spectrometry (Prentice *et al.*, 2014). In this study, Ti is particularly concentrated in small nodules with size ranging from 100 to 500 nm. In both heterococcoliths, Ti nodules are not correlated with Ca-rich spots but rather located at the junction between CaCO₃ crystals. Ti nodules could possibly be nanoscale Ti-rich clay particles, which size (down to 100 nm) is consistent with the clay particles observed by Skovbjerg *et al.* (2012). However, these Ti-rich clay nodules are different from the central area clay, highlighting at least two sources of contamination in our results.

Contamination from clays cannot be entirely avoided with the methodology we adopted to isolate heterococcoliths in the present study. We deliberately avoided chemical reagents in order to circumvent any potential cleaning contamination of the specimens. However, the advantage of the high-resolution mapping method adopted here is that it allows the unambiguous identification of contaminated zones, and therefore the selection of uncontaminated zones such as ROI 1 (Fig. 6) for further discussions on heterococcolith primary geochemical composition.

Diagenetic contribution

During diagenesis, heterococcoliths can be etched and/or overgrown. Overgrowth builds upon primary heterococcolith crystals (Adelseck *et al.*, 1973), and tends to preserve the primary crystalline organisation. In Fig. 1B, the primary crystalline organisation of *W. britannica* is easily observable even if several monocrystals are thicker at the rim than at the inner tube due to overgrowth. During diagenesis, heterococcolith crystals larger than 1 µm and large heterococcoliths tend to overgrow whereas small crystals, small heterococcoliths and broken pieces of heterococcoliths tend to dissolve (Adelseck *et al.*, 1973). Overgrowth of an heterococcolith from its etched parts was not observed and thus not further considered in this discussion. Dissolved CaCO₃ from heterococcoliths and other carbonate sources is mixed with the diagenetic fluids of the bulk rock, which is also composed of clay. Hence, the overgrown parts of heterococcoliths are likely to have different elemental compositions than the original one. In marlstones that contain clay, diagenetic fluids are typically enriched in metals. The absolute and relative *i*/Ca concentration maps of Wbrit1 and Wbrit2 show that heterococcoliths are enriched in K, Fe, Cu, Zn and Rb on the outermost rims that are interpreted as overgrown parts (Fig. 10). Those elements are incorporated in overgrown calcite on one or both sides of the heterococcoliths or between the proximal and distal shields (Fig. 10). In both heterococcoliths, radial overgrowth is also observed and is located between crystals, which form edges offering crystallization loci. These features define a specific pattern of overgrowth on the edges and between crystals, where K, Fe, Cu, Zn and Rb are concentrated.

One of the most intriguing observation in the present study was the distinctive distribution of Mn. Mn²⁺ has strong affinities with carbonate and may substitute Ca²⁺ during calcification (Paquette & Reeder, 1995; Astilleros *et al.*, 2002). It is often considered as a diagenetic contaminant resulting from secondary incorporation in carbonate fossils (Boyle *et al.*, 1983; Pena *et al.*, 2008). In the present XRF maps, the distribution of Mn in Wbrit1 and Wbrit2 is closer to Ca and Sr than to any other element (Fig. 3) questioning the often-assumed diagenetic origin of Mn in calcite. The Mn and Mn/Ca maps (Figs. 3 and 7) display with great

detail an outer Mn ring with clockwise orientation as well as anticlockwise radial features, which are more visible in the upper right corner of each heterococcolith. Assuming a proximal view of the heterococcolith, the former ring could correspond to the proximal shield with clockwise (dextrogyre) orientation of the calcite crystals while the latter could correspond to the distal shield with anticlockwise (laevogyre) orientation of the calcite crystals (Fig. 1A). This distinctive organisation suggests that Mn is more concentrated in one or the other shield. This could be due to abiotic diagenetic overgrowth on the shields surfaces and/or between both shields (Fig. 11), rather than zonal biological incorporation. A differential enrichment in Mn in only part of a given monocrystal seems indeed difficult to explain during heterococcolithogenesis. Abiotic experiments have shown that Mn-rich carbonate has affinities with $\{10\bar{1}4\}$ crystal surfaces (Astilleros *et al.*, 2002), which actually correspond to the orientations of shield surfaces in *Watznaueria* (Saruwatari *et al.*, 2008). This suggests that Mn is present in heterococcolith in the form of Mn-CaCO₃ rather than Mn-oxides.

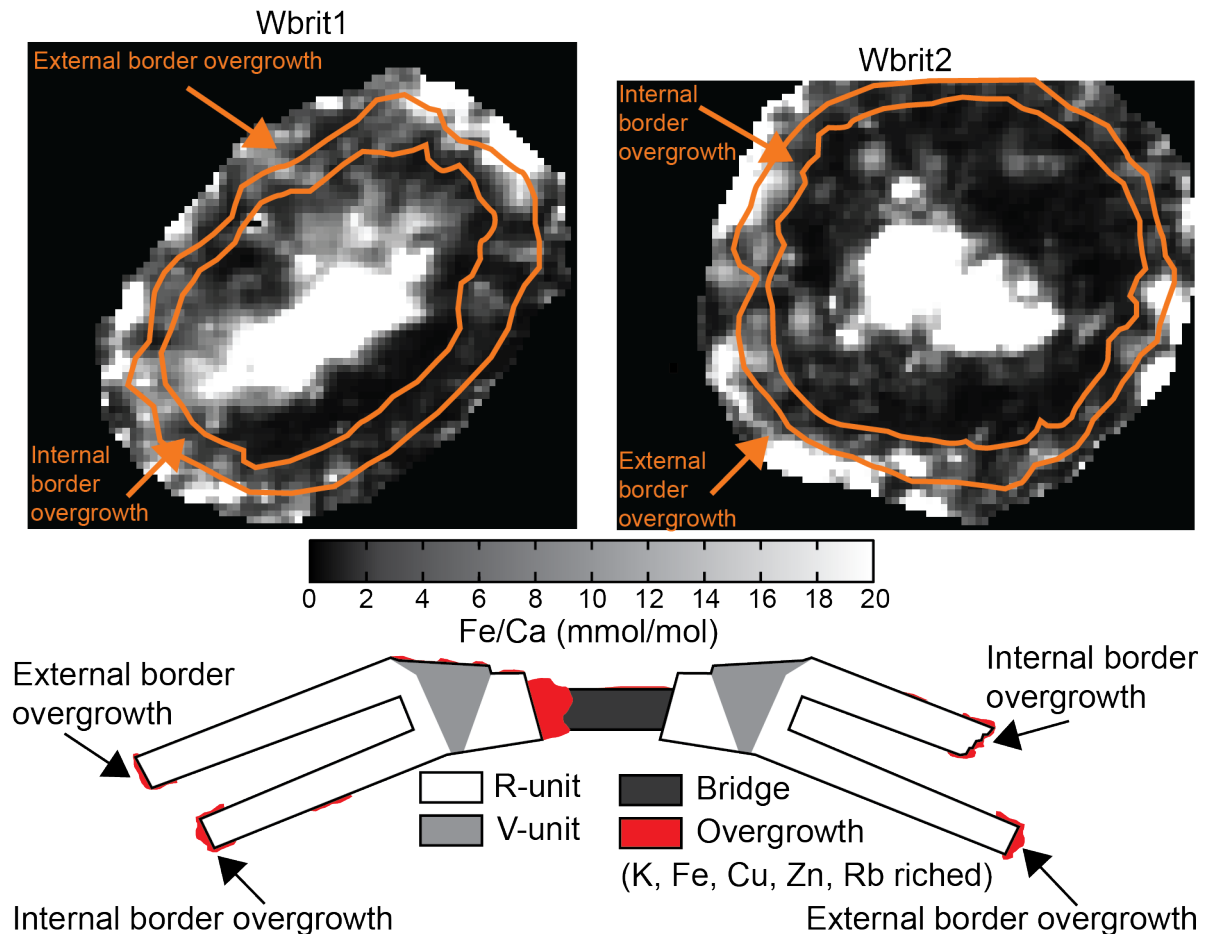


Figure 10: Diagenetic model of K, Fe, Cu, Zn and Rb overgrowth based on the Wbrit1 and Wbrit2 Fe/Ca maps (Fig. 9). The overgrowth is concentrated on the shields borders, in the central area and some nodules covering the proximal and distal shields. Overgrowth at the connection between R- and V-units is not shown on the lateral view scheme but was also observed in the Wbrit1 and Wbrit2 Fe/Ca maps.

As a concluding remark to this part of the discussion, we recommend that heterococcoliths are carefully selected and cleaned prior to any analysis focusing on K, Mn, Fe, Ti, V, Cr, Cu, Zn

and Rb elemental composition and/or their isotopes. Oppositely Ca, Sr, S, Cl and Br appear to be affected by neither clay contamination nor secondary diagenetic processes in the heterococcoliths studied here, and are therefore of potential use in palaeobiology and palaeoceanography.

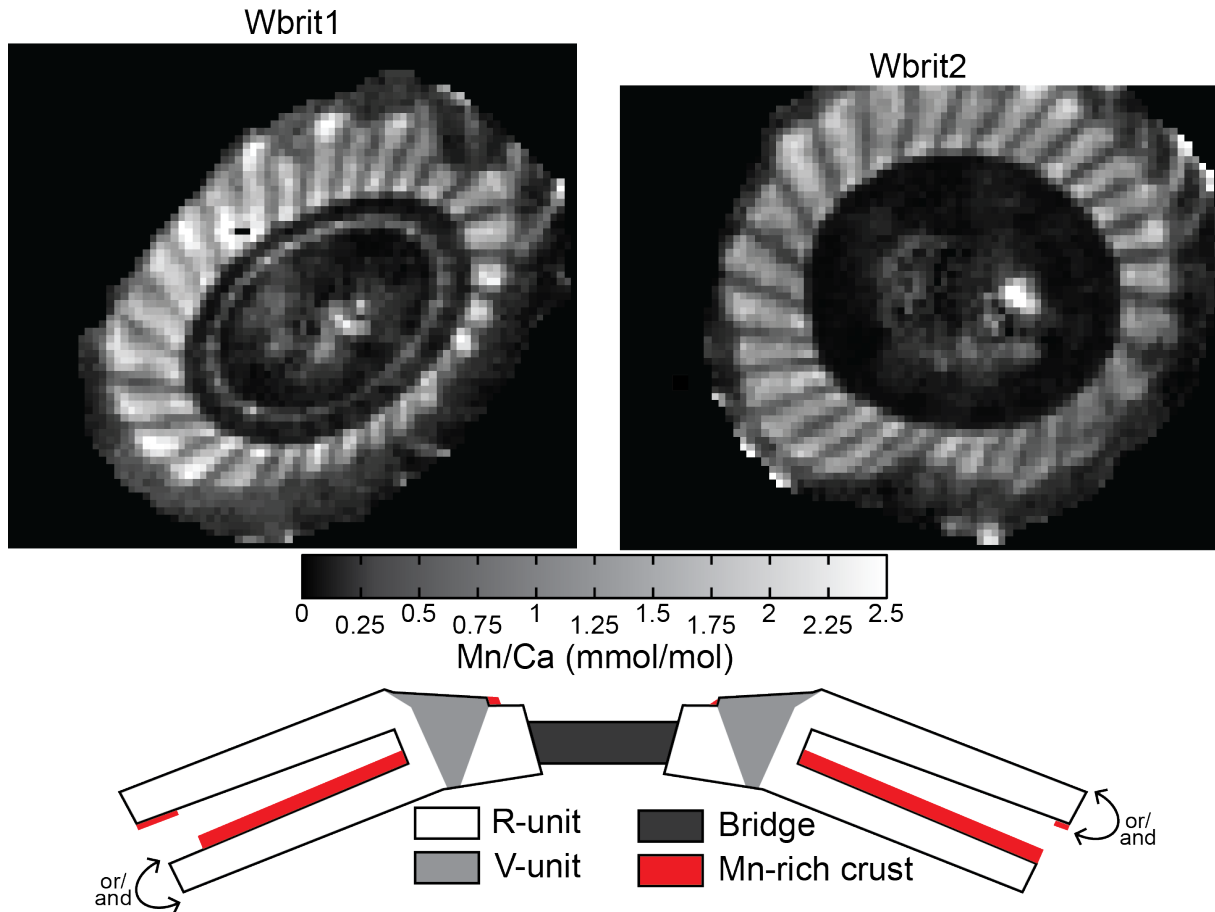


Figure 11: Diagenetic model of Mn-rich carbonate overgrowth based on the Wbrit1 and Wbrit2 Mn/Ca maps (Fig. 7). The Mn-rich overgrowth is concentrated between the shields and at the connection between R- and V-units in the inner part of the heterococcoliths.

Trace elements identified as potential environmental proxies

Possible salinity proxy based on chlorine and bromine in heterococcoliths

The model traditionally used in calcite elemental geochemistry is based on cations, with Ca^{2+} being replaced by other cations in the calcite lattice like Sr^{2+} or Mg^{2+} (Finch & Allison, 2007). Anion geochemistry in biogenic calcite, however, is poorly studied and there is, to our best knowledge, no model available for anion incorporation and exchange in calcite. Cl and Br are homogeneously present in our maps. Ca^{2+} and CO_3^{2-} form the crystalline lattice of CaCO_3 . The present data cannot directly determine whether Cl^- and Br^- actually replace CO_3^{2-} in the calcite lattice. If Cl and Br did replace CO_3^{2-} in the calcite lattice, their distribution in the heterococcolith should be similar to that of Ca, which is not the case. Because of the differences in Cl and Br distribution and that of Ca, we hypothesize instead that Cl and Br are impurities in interstitial nano-domains.

In the coccolithophore species *Coccolithus pelagicus*, a Cl⁻ inward-rectifying current (also applicable to Br⁻) has been observed in the cell plasma membrane, but this ion channel does not mediate large osmo-regulation and likely equilibrates HCO₃⁻ uptake and membrane voltage (Taylor & Brownlee, 2003; Mackinder *et al.*, 2011). HCO₃⁻ is then used by the cell for photosynthesis and heterococcolithogenesis (Mackinder *et al.*, 2011). Hence, once HCO₃⁻ is consumed, we can confidently hypothesize that there is an influx of anions through the cell wall that compensates for the loss of HCO₃⁻ and activates the Cl⁻ channel again. This anion influx that compensates the loss of HCO₃⁻ is most likely sustained by Cl⁻, the most abundant anion in seawater. This could be a passive diffusive influx through the cell wall by osmotic regulation or active pumping. Inward and outward Cl⁻ fluxes would then result in an active cyclic movement of Cl⁻ leading to a constant [Cl⁻] in the cell at the scale of heterococcolith formation. This hypothesis is likely also applicable to Br⁻, which has the same behaviour as Cl⁻ in coccolithophore cells (Taylor & Brownlee, 2003).

Because Cl and Br are most likely impurities in heterococcolith calcite, they are not biologically concentrated in the heterococcolith and would therefore depend on the coccolithophore cytoplasm [Cl⁻] and [Br⁻]. Since there is a direct link between seawater [Cl⁻] and [Br⁻] and coccolithophore cytoplasm [Cl⁻] and [Br⁻] as described earlier, heterococcolith Cl and Br may prove useful as seawater [Cl⁻] and [Br⁻] proxies. Cl⁻ is the most abundant anion in seawater, and salinity is directly related to seawater [Cl⁻] (Adkins *et al.*, 2002). Thus, if heterococcolith Cl and Br prove to be good seawater [Cl⁻] and [Br⁻] proxies, heterococcolith Cl and Br may in turn be an interesting tool in the establishment of a salinity proxy.

Record of heterococcolithogenesis based on sulfur

The strong similarity between the distribution of Cl and S in heterococcolith could lead to the hypothesis that heterococcolith S/Ca has potential as a seawater [S] proxy, an important element in Earth geochemical dynamics (Berner, 2006). Unfortunately, S is present in many biological processes occurring inside the cell during heterococcolithogenesis, involving polysaccharides (PS) that transport Ca²⁺ to a base plate where the heterococcolith is built (Westbroek *et al.*, 1983). In *Pleurochrysis carterae* and *Emiliana huxleyi* for instance, the polysaccharide known as PS3 is a sulfated galacturonomannan that is active in crystal growth and shaping (Marsh *et al.*, 2002). Some polysaccharides have been observed trapped inside the heterococcolith calcite lattice (Takahashi *et al.*, 2002). Consequently, we interpret the presence of S as PS residues inside heterococcoliths. Because of the disequilibrium between heterococcoliths and seawater caused by biological concentration during heterococcolith formation, S/Ca is not useful as a tracer for seawater composition. The presence of S in *W. britannica* nonetheless suggests that coccolithophores used sulfated PS for heterococcolithogenesis for at least 170 Myr. This is of interest because further isotopic analysis of S trapped within heterococcoliths may deliver palaeobiological information on heterococcolithogenesis.

New insights of Sr/Ca in W. britannica

In both Wbrit1 and Wbrit2, Sr/Ca maps display detailed features that follow *W. britannica*'s crystalline organisation (Figs. 1, 7 and 12). Sr/Ca distribution perfectly reflects the arrangement of calcite crystals in the V-units of the mid-tube elements. Sr/Ca distribution in

calcite crystals in the R-units of the rim are less distinguishable, a result of overlapping of the R-unit crystals in the distal shield and/or the fact that the shields' crystals have different orientations, *i.e.* clockwise for the proximal shield and anti-clockwise for the distal shield in distal view (Fig. 1A). Conversely, limits between mid-tube elements are easily identifiable because those elements are made of V-unit monocrystals with vertical walls.

Although Sr/Ca maps clearly depict the organisation of calcite crystals in heterococcoliths, the Sr/Ca ratio varies only slightly between R- and V-units, with a mean value of 0.35 ± 0.14 (1σ) mmol/mol and 0.36 ± 0.15 (1σ) mmol/mol (Fig. 12). This important result confirms previous observations (Stoll and Ziveri, 2004) that the partitioning coefficient of strontium D_{Sr} between calcite and cytoplasm does not depend on the crystal growth direction. Despite the differences in crystal axes and shapes between V- and R-units (Saruwatari *et al.*, 2008; Saruwatari *et al.*, 2011), the factor controlling Sr incorporation is the elongation along the c-axis in both V- and R-units (Payne *et al.*, 2006).

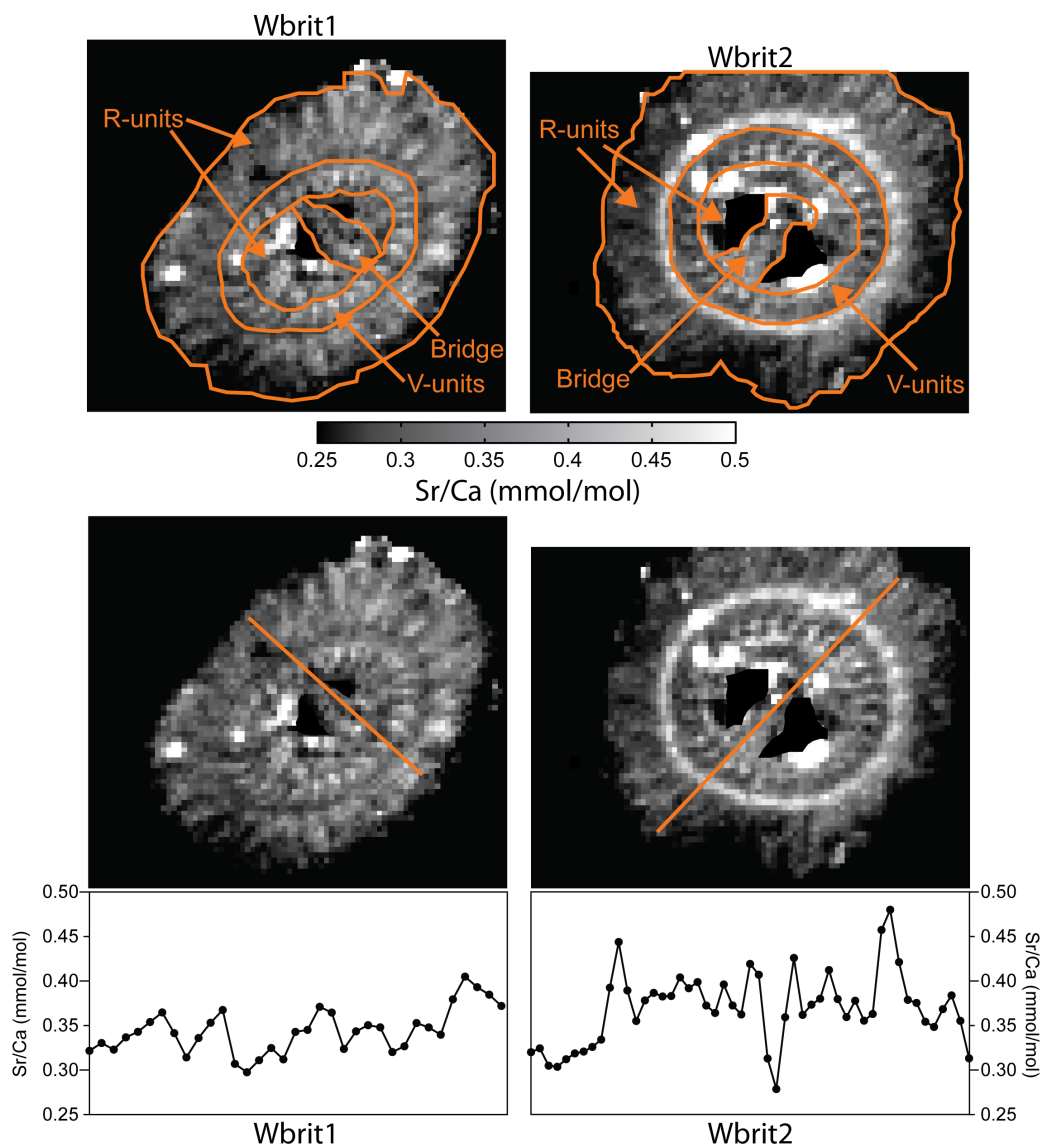


Figure 12: Identification of the *W. britannica* *Wbrit1* and *Wbrit2* crystal organisations in the Sr/Ca maps (in mmol/mol) and Sr/Ca transects showing the low variations in Sr/Ca along the minor axis.

Sr/Ca in *W. britannica* is twice to 12 times (Table 1) lower than in modern and Cenozoic species, which are characterized by a Sr/Ca ranging from 0.8 to 4 mmol/mol (Stoll & Bains, 2003; Stoll & Ziveri, 2004; Dedert *et al.*, 2012; Dedert *et al.*, 2014; Prentice *et al.*, 2014). In one hand, Sr/Ca is homogenous in Wbrit1 and Wbrit2 (Fig. 12). On the other hand, calcite overgrowth in heterococcoliths is not homogeneous (Fig. 1B) and is documented to lower the original Sr/Ca (Dedert *et al.*, 2014; Prentice *et al.*, 2014). Hence, we consider that calcite overgrowth in Wbrit1 and Wbrit2 has a minor to negligible impact on Sr/Ca. In the absence of published *W. britannica* Sr/Ca to compare our results with, two hypotheses explaining the low Sr/Ca of our *W. britannica* are presented and could both occur together: i) the cellular physiology of Mesozoic coccolithophores and/or ii) a low cellular growth rate.

Elemental ratio	Palaeoceanographic proxy	Palaeobiologic proxy	Diagenetic or sedimentary contamination
Sr/Ca		Sulphated polysaccharides	
Cl/Ca	Salinity ?		
K/Ca			Diagenesis and clays
Ti/Ca			Diagenesis and clays
V/Ca			Diagenesis and clays
Cr/Ca			Diagenesis and clays
Mn/Ca			Diagenesis
Fe/Ca			Diagenesis and clays
Cu/Ca			Diagenesis and clays
Zn/Ca			Diagenesis and clays
Br/Ca	Salinity ?		
Rb/Ca			Diagenesis and clays
Sr/Ca	Productivity		

Table 2: Concise table resuming the interest of the different element ratios presented for palaeoceanographic proxy, palaeobiologic proxy and/or diagenetic or sedimentary contamination.

Watznaueria are the most abundant heterococcoliths in the fossil record from the Middle Jurassic until the end of the Cretaceous and *W. britannica* is particularly abundant in Middle and Upper Jurassic sediments. Sedimentary evidence (microlaminae) of blooms of this species is documented (Lees *et al.*, 2004) and an affinity for eutrophic conditions was proposed (Lees *et al.*, 2006; Suchéras-Marx *et al.*, 2015) without distinguishing morphotypes. Such high abundances in the fossil record are more likely related to a ubiquitous and eurytopic ecology. In comparison to modern environments, *W. britannica* in the Middle Jurassic is comparable to *E. huxleyi* in term of dominance in the nannofossil assemblage even if their morphology, size and size range are completely different. *W. britannica* has very low Sr/Ca with respect to *E. huxleyi* and other modern and Cenozoic species. These exceptionally low Sr/Ca values for the dominant Mesozoic placolith could be related to different cellular physiology between Mesozoic forms and Cenozoic to modern forms. The Cretaceous-Paleogene mass extinction, which has led to the most important turnover in coccolithophore evolutionary history (Bown, 2005), could have led to the extinction of the most Sr-depleted heterococcoliths replaced by coccolithophore producing Sr-enriched heterococcoliths. There is a need to establish the behaviour and geochemistry of Mesozoic nannofossils somewhat independently of what we assume from modern/Cenozoic taxa. In particular, new Sr/Ca

analyses on Mesozoic survivors still present in modern oceans, namely *Tergestiella adriatica* (Hagino *et al.*, 2015), could help to test this hypothesis.

Both *W. britannica* specimens studied here belong to a large-sized morphotype and different studies focusing on the palaeoecology of this species have shown that large-size morphotypes were adapted to stable and relatively oligotrophic environmental conditions (Olivier *et al.*, 2004; Giraud *et al.*, 2006; Giraud *et al.*, 2009). Today, extant heterococcolith species adapted to oligotrophic conditions (e.g. *Umbilicosphaera sibogae sibogae*) are also characterized by low cell growth rates and low D_{Sr} (Stoll *et al.*, 2002), leading to low Sr/Ca. This also applies to heterococcoliths that are usually characterized by high growth rates during the stationary phase of the population growth (Rickaby *et al.*, 2002). Low Sr/Ca in *E. huxleyi* was recorded in nutrient-poor culture experiments (Stoll *et al.*, 2007b), stationary-phase population growth in culture experiments (Rickaby *et al.*, 2002), and in the Eastern Mediterranean Sea, which is considered as a “nutrient desert” (Auliahherliaty *et al.*, 2009). Hence, low Sr/Ca in our *W. britannica* suggests an adaptation to oligotrophic conditions of the large morphotype, as proposed by Giraud *et al.* (2006, 2009). A summary of potential uses of heterococcolith elemental geochemistry for palaeoceanography, palaeobiology and/or identification of diagenesis and clay contamination is given in Table 2.

CONCLUSION

We have confidently identified and mapped 14 elements in two Middle Jurassic *W. britannica* heterococcoliths using nanoscale XRF mapping. Amongst those 14 elements, K, Ti, V, Fe, Cu, Zn and Rb are linked to clay contamination and diagenetic overprint whereas Mn is present in calcite overgrowth, likely in the form of Mn-rich $CaCO_3$. Presence of S is interpreted as a residue of sulfated polysaccharides, which mediate crystal growth and shape in some modern coccolithophores. Cl and Br are also present in heterococcoliths, more likely in interstitial nano-domains than as substitutes for CO_3^{2-} . Heterococcolith Cl content may be interesting as a salinity proxy, but this would require demonstration of a linear correlation between [Cl] in heterococcoliths and [Cl⁻] in seawater in culture experiments. Finally, Sr/Ca is unusually low (i.e. 0.35 mmol/mol) in the analysed *W. britannica* compared to Cenozoic/modern species. This low Sr/Ca could be related to different cellular physiology in Mesozoic coccolithophores, or it could also be the result of low growth rates in those individuals. The present study on fossilised heterococcoliths helps to identify the relative contributions of contamination, diagenesis and biology to the final elemental composition. This study, alongside Prentice *et al.* (2014), provides new insights in heterococcolith chemical composition and applicability to palaeoceanography but further effort is needed in terms of culture studies, cell biology and crystallographic studies.

Acknowledgements

We thank the ESRF scientific committee for selecting and funding the EC-811 experiment. We are grateful to Emanuela Mattioli for her support in the early stage of the project, Christophe Chamot at PLATIM for methodological help, Yves Gally and Bertrand Devouard for SEM picture acquisition, Julia Kende and Simon Seguy for Matlab algorithms, Anne-

Sabine Grosjean for figures, Sylvain Pichat, Jorijntje Henderiks, Daniela Schmidt, Jackie Lees and Glen Wheeler for interesting discussions on the methods and results, and Nathaniel Dahan and Clara Bolton for English revision. We also thank the reviewers and the editors for greatly improving the paper. Pre-print version.

References

- Adelseck CG, Geehan GW, Roth PH (1973) Experimental evidence for the selective dissolution and overgrowth of calcareous nanofossils during diagenesis. *Geological Society of America Bulletin*, **84**, 2755-2762.
- Adkins JF, McIntyre K, Schrag DP (2002) The salinity, temperature, and $\delta^{18}\text{O}$ of the glacial deep ocean. *Science*, **298**, 1769-1773.
- Astilleros JM, Pina CM, Fernandez-Daz L, Putnis A (2002) Molecular-scale surface processes during the growth of calcite in the presence of manganese. *Geochimica et Cosmochimica Acta*, **66**, 3177-3189.
- Auliaherliaty L, Stoll HM, Ziveri P, Malinverno E, Triantaphyllou M, Stravarakakis S, Lykousis V (2009) Coccolith Sr/Ca ratios in the eastern Mediterranean: Production versus export processes. *Marine Micropaleontology*, **73**, 196-206.
- Berner RA (2006) GEOCARBSULF: A combined model for Phanerozoic atmospheric O_2 and CO_2 . *Geochimica et Cosmochimica Acta*, **70**, 5653-5664.
- Bown PR (1998) *Calcareous nanofossil biostratigraphy*. British Micropaleontological Society Publication Series, Chapman and Hall (Kluwer Academic Publishers), Dordrecht.
- Bown PR (2005) Selective calcareous nanoplankton survivorship at the Cretaceous-Tertiary boundary. *Geology*, **33**, 653-656.
- Bown PR, Young JR (1998) Technique. In: *Calcareous nanofossil biostratigraphy* (ed. Bown PR). British Micropaleontological Society Publication Series, Chapman and Hall (Kluwer Academic Publishers), Dordrecht, pp. 16-28.
- Boyle EA (1983) Manganese carbonate overgrowths on foraminifera tests. *Geochimica et Cosmochimica Acta*, **47**, 1815-1819.
- Candelier Y, Minoletti F, Probert I, Hermoso M (2013) Temperature dependence of oxygen isotope fractionation in coccolith calcite: A culture and core top calibration of the genus *Calcidiscus*. *Geochimica et Cosmochimica Acta*, **100**, 264-281.
- Cros L, Estrada M (2013) Holo-heterococcolithophore life cycles: ecological implications. *Marine Ecology Progress Series*, **492**, 57-68.
- Dedert M, Stoll HM, Kars S, Young JR, Shimizu N, Kroon D, Lourens L., Ziveri P (2014) Temporally variable diagenetic overgrowth on deep-sea nanofossil carbonates across Palaeogene hyperthermals and implications for isotopic analyses. *Marine Micropaleontology*, **107**, 18-31.
- Dedert M, Stoll HM, Kroon D, Shimizu N, Kanamaru K, Ziveri P (2012) Productivity response of calcareous nanoplankton to Eocene Thermal Maximum 2 (ETM2). *Climate of the Past*, **8**, 977-993.
- Dudley WC, Goodney DE (1979) Oxygen isotope content of coccoliths grown in culture. *Deep-Sea Research Part A. Oceanographic Research Papers*, **26**, 495-503.

- Dudley WC, Blackwelder P, Brand L, Duplessy J-C (1986) Stable isotopic composition of coccoliths. *Marine Micropaleontology*, **10**, 1-8.
- Dunkley Jones T, Bown PR, Pearson PN (2009) Exceptionally well preserved upper Eocene to lower Oligocene calcareous nannofossils (Prymnesiophyceae) from the Pande Formation (Kilwa Group), Tanzania. *Journal of Systematic Palaeontology*, **7**, 359-411.
- Finch AA, Allison, N (2007) Coordination of Sr and Mg in calcite and aragonite. *Mineralogical Magazine*, **71**, 539-552.
- Geisen M, Billard C, Broerse ATC, Cros L, Probert I, Young JR (2002) Life-cycle associations involving pairs of holococcolithophorid species : intraspecific variation or cryptic speciation?. *European Journal of Phycology*, **37**, 531-550.
- Giraud F, Pittet B, Mattioli E, Audouin V (2006) Paleoenvironmental controls on the morphology and abundance of the coccolith *Watznaueria britannica* (Late Jurassic, southern Germany). *Marine Micropaleontology*, **60**, 205-225.
- Giraud F, Courtinat B, Atrops F (2009) Spatial distribution patterns of calcareous nannofossils across the Callovian-Oxfordian transition in the french subalpine basin. *Marine Micropaleontology*, **72**, 129-145.
- Halloran PR, Rust N, Rickaby REM (2009) Isolating coccoliths from sediment for geochemical analysis. *Geochemistry, Geophysics, Geosystems*, **10**, Q03001.
- Hagino K, Young JR, Bown PR, Godrijan J, Kulhanek DK, Kogame K, Horiguchi T (2015) Re-discovery of a "living fossil" coccolithophore from the coastal waters of Japan and Croatia. *Marine Micropaleontology*, **116**, 28-37.
- Ho T-Y, Quigg A, Finkel ZV, Milligan AJ, Wyman K, Falkowski PG, Morel FMM (2003) The elemental composition of some marine phytoplankton. *Journal of Phycology*, **39**, 1145-1159.
- Köster HM (1996) Mineralogical and chemical heterogeneity of three standard clay mineral samples. *Clay Minerals*, **31**, 417-422.
- Lees JA, Bown PR, Young JR (2006) Photic zone palaeoenvironments of the Kimmeridge Clay Formation (Upper Jurassic, UK) suggested by calcareous nannoplankton palaeoecology. *Palaeogeography, Palaeoclimatology, Palaeoecology*, **235**, 110-134.
- Mackinder L, Wheeler G, Schroeder D, von Dassow P, Riebesell U, Brownlee C (2011) Expression of biomineralization-related ion transport genes in *Emiliania huxleyi*. *Environmental Microbiology*, **13**, 3250-3265.
- Marsh ME, Ridall AL, Azadi P, Duke PJ (2002) Galacturonomannan and Golgi-derived membrane linked to growth and shaping of biogenic calcite. *Journal of Structural Biology*, **139**, 39-45.
- Minoletti F, Hermoso M, Gressier V (2009) Separation of sedimentary micron-sized particles for palaeoceanography and calcareous nannoplankton biogeochemistry. *Nature Protocols*, **4**, 14-24.
- Müller MN, Kisakürek B, Buhl D, Gutperlet R, Kolevica A, Riebesell U, Stoll HM, Eisenhauer A (2011) Response of the coccolithophores *Emiliania huxleyi* and *Coccolithus braarudii* to changing seawater Mg²⁺ and Ca²⁺ concentrations: Mg/Ca, Sr/Ca ratios and $\delta^{44/40}\text{Ca}$, $\delta^{26/24}\text{Mg}$ of coccolith calcite. *Geochimica et Cosmochimica Acta*, **75**, 2088-2102.

- Olivier N, Pittet B, Mattioli E (2004) Palaeoenvironmental control on sponge-microbialite reefs and contemporaneous deep-shelf marl-limestone deposition (Late Oxfordian, southern Germany). *Palaeogeography, Palaeoclimatology, Palaeoecology*, **212**, 233-263.
- Paquette J, Reeder RJ (1995) Relationship between surface structure, growth mechanism, and trace element incorporation in calcite. *Geochimica et Cosmochimica Acta*, **59**, 735-749.
- Payne VE, Rickaby REM, Benning LG, Shaw S (2008) Calcite crystal growth orientation: implications for trace metal uptake into coccoliths. *Mineralogical Magazine*, **72**, 269-272.
- Pena LD, Cacho I, Calvo E, Pelejero C, Eggins S, Sadekov A (2008) Characterization of contaminant phases in foraminifera carbonates by electron microprobe mapping. *Geochemistry, Geophysics, Geosystems*, **9**, Q07012.
- Prentice K, Dunkley Jones T, Lees J, Young JR, Bown PR, Langer G, Fearn S, EIMF (2014) Trace metal (Mg/Ca and Sr/Ca) analyses of single coccoliths by Secondary Ion Mass Spectrometry. *Geochimica et Cosmochimica Acta*, **146**, 90-106.
- Ra K, Kitagawa H, Shiraiwa Y (2010) Mg isotopes and Mg/Ca values of coccoliths from cultured specimens of the species *Emiliana huxleyi* and *Gephyrocapsa oceanica*. *Marine Micropaleontology*, **77**, 119-124.
- Rickaby REM, Schrag DP, Zondervan I, Riebesell U (2002) Growth rate dependence of Sr incorporation during calcification of *Emiliana huxleyi*. *Global Biochemical Cycles*, **16**, 1006.
- Sadekov AY, Eggins SM, De Deckker P (2005) Characterization of Mg/Ca distributions in planktonic foraminifera species by electron microprobe mapping. *Geochemistry, Geophysics, Geosystems*, **6**, Q12P06.
- Saruwatari K, Ozaki N, Nagasawa H, Kogure T (2008) Comparison of crystallographic orientations between living (*Emiliana huxleyi* and *Gephyrocapsa oceanica*) and fossil (*Watznaueria barnesiae*) coccoliths using electron microscopes. *American Mineralogist*, **93**, 1670-1677.
- Saruwatari K, Tanaka Y, Nagasawa H, Kogure T (2011) Crystallographic variability and uniformity in Cretaceous heterococcoliths. *European Journal of Mineralogy*, **23**, 519-528.
- Schlanger O, Douglas WRG, Lancelot Y, Moore TC, Roth PH (1973) Fossil preservation and diagenesis of pelagic carbonates from the Magellan Rise, central North Pacific Ocean. In: *Initial Reports of the Deep Sea Drilling Project* (eds. Winterer EL, Ewing JJ *et al.*). U.S. Government Printing Office, Washington, pp. 407-427.
- Siesser WG (1977) Chemical composition of calcareous nanofossils. *South African Journal of Science*, **73**, 283-285.
- Skovbjerg LL, Hassenkam T, Makovicky E, Hem CP, Yang M, Bovet N, Stipp SLS (2012) Nano sized clay detected on chalk particle surfaces. *Geochimica et Cosmochimica Acta*, **99**, 57-70.
- Solé VA, Papillon E, Cotte M, Walter P, Susini J (2007) A multiplatform code for the analysis of energy-dispersive X-ray fluorescence spectra. *Spectrochimica Acta B*, **62**, 63-68.
- Stanley SM, Ries JB, Hardie LA (2005) Seawater chemistry, coccolithophore population growth, and the origin of Cretaceous chalk. *Geology*, **33**, 593-596.
- Stoll HM, Bains S (2003) Coccolith Sr/Ca records of productivity during the Paleocene-Eocene thermal maximum from the Weddell Sea. *Paleoceanography*, **18**, 1049.

- Stoll HM, Schrag DP (2000) Coccolith Sr/Ca as a new indicator of coccolithophorid calcification and growth rate. *Geochemistry, Geophysics, Geosystems*, **1**, 1006.
- Stoll HM, Shimizu N (2009) Micropicking of nanofossils in preparation for analysis by secondary ion mass spectrometry. *Nature Protocols*, **4**, 1038-1043.
- Stoll HM, Ziveri P (2002) Separation of monospecific and restricted coccolith assemblages from sediments using differential settling velocity. *Marine Micropaleontology*, **46**, 209-221.
- Stoll HM, Ziveri P (2004) Coccolithophorid-based geochemical paleoproxies. In: *Coccolithophores - From molecular processes to global impact* (eds. Thierstein HR, Young JR). Springer-Verlag, Berlin Heidelberg, pp. 529-562.
- Stoll HM, Encinar JR, Alonso JIG, Rosenthal Y, Probert I, Klaas C (2001) A first look at paleotemperature prospects from Mg in coccolith carbonate: Cleaning techniques and culture measurements. *Geochemistry, Geophysics, Geosystems*, **2**, 2000GC000144.
- Stoll HM, Klaas CM, Probert I, Ruiz Encinar J, Garcia Alonso JI (2002) Calcification rate and temperature effects on Sr partitioning in coccoliths of multiple species of coccolithophorids in culture. *Global and Planetary Change*, **34**, 153-171.
- Stoll HM, Shimizu N, Arevalos A, Matell N, Banasiak A, Zeren S (2007a) Insights on coccolith chemistry from a new ion probe method for analysis of individually picked coccoliths. *Geochemistry, Geophysics, Geosystems*, **8**, Q06020.
- Stoll HM, Ziveri P, Shimizu N, Conte M, Theroux S (2007b) Relationship between coccolith Sr/Ca ratios and coccolithophore production and export in the Arabian Sea and Sargasso Sea. *Deep-Sea Research Part II: Tropical Studies in Oceanography*, **54**, 581-600.
- Suchéras-Marx B, Giraud F, Mattioli E, Escarguel G (2015) Paleoenvironmental and paleobiological origins of coccolithophorid genus *Watznaueria* emergence during the Late Aalenian-Early Bajocian. *Paleobiology*, **41**, 415-435.
- Suchéras-Marx B, Guihou A, Giraud F, Lécuyer C, Allemand P, Pittet B, Mattioli E (2012) Impact of the Middle Jurassic diversification of *Watznaueria* (coccolith-bearing algae) on the carbon cycle and $\delta^{13}\text{C}$ of bulk marine carbonates. *Global and Planetary Change*, **86-87**, 92-100.
- Takahashi J-i, Fujiwara S, Kikyo M, Hirokawa Y, Tsuzuki M (2002) Discrimination of the cell surface of the coccolithophorid *Pleurochrysis haptanemofera* from Light Scattering and Fluorescence after Fluorescein-Isothiocyanate-Labeled Lectin staining measured by Flow Cytometry. *Marine Biotechnology*, **4**, 94-101.
- Taylor AR, Brownlee C (2003) A novel Cl^- inward-rectifying current in the plasma membrane of the calcifying marine phytoplankton *Coccolithus pelagicus*. *Plant Physiology*, **131**, 1391-1400.
- Taylor AR, Russell MA, Harper GM, Collins TFT, Brownlee C (2007) Dynamics of formation and secretion of heterococcoliths by *Coccolithus pelagicus* ssp. *braarudii*. *European Journal of Phycology*, **42**, 125-136.
- Thierstein HR, Young JR (2004) *Coccolithophores - From molecular processes to global impact*. Springer-Verlag, Berlin Heidelberg.
- Tripati AK, Eagle RA, Thiagarajan N, Gagnon AC, Bauch H, Halloran PR, Eiler JM (2010) ^{13}C - ^{18}O isotope signatures and 'clumped isotope' thermometry in foraminifera and coccoliths. *Geochimica et Cosmochimica Acta*, **74**, 5697-5717.

- Westbroek P, De Jong EW, Van Der Wal P, Borman AH, De Vrind JPM, Kok D, De Bruijn WC, Parker SB (1984) Mechanism of calcification in the marine alga *Emiliana huxleyi*. *Philosophical Transactions of the Royal Society Serie B*, **304**, 435-444.
- Winter A, Siesser WG (1994) *Coccolithophores*. Cambridge University Press, Cambridge.
- Young JR, Bown PR (1991) An ontogenetic sequence of coccoliths from the Late Jurassic Kimmeridge clay of England. *Palaeontology*, **34**, 843-850.
- Young JR, Bergen JA, Bown PR, Burnett JA, Fiorentino A, Jordan RW, Kleijne A, Van Niel BE, Romein AJT, Von Salis K (1997) Guidelines for coccolith and calcareous nannofossil terminology. *Palaeontology*, **40**, 875-912.